JCI insight

RESEARCH ARTICLE

Mouse model of Gram-negative prosthetic joint infection reveals therapeutic targets

John M. Thompson,[1] Robert J. Miller,[2] Alyssa G. Ashbaugh,[2] Carly A. Dillen,[2] Julie E. Pickett,[3] Yu Wang,[2] Roger V. Ortines,[2] Robert S. Sterling,[1] Kevin P. Francis,[4,5] Nicholas M. Bernthal,[5] Taylor S. Cohen,[6] Christine Tkaczyk,[6] Li Yu,[7] C. Kendall Stover,[6] Antonio DiGiandomenico,[6] Bret R. Sellman,[6] Daniel L.J. Thorek,[3,8] and Lloyd S. Miller[1,2,9,10]

[1]Department of Orthopaedic Surgery, [2]Department of Dermatology, and [3]Department of Radiology and Radiological Sciences, Division of Nuclear Medicine, Johns Hopkins University School of Medicine, Baltimore, Maryland, USA. [4]PerkinElmer, Hopkinton, Massachusetts, USA. [5]Department of Orthopaedic Surgery, David Geffen School of Medicine at UCLA, Santa Monica, California, USA. [6]Department of Infectious Diseases and [7]Statistical Sciences, MedImmune, Gaithersburg, Maryland, USA. [8]Cancer Molecular and Functional Imaging Program, Department of Oncology, Sidney Kimmel Comprehensive Cancer Center, and [9]Department of Medicine, Division of Infectious Diseases, Johns Hopkins University School of Medicine, Baltimore, Maryland, USA. [10]Department of Materials Science and Engineering, Johns Hopkins University, Baltimore, Maryland, USA.

Bacterial biofilm infections of implantable medical devices decrease the effectiveness of antibiotics, creating difficult-to-treat chronic infections. Prosthetic joint infections (PJI) are particularly problematic because they require prolonged antibiotic courses and reoperations to remove and replace the infected prostheses. Current models to study PJI focus on Gram-positive bacteria, but Gram-negative PJI (GN-PJI) are increasingly common and are often more difficult to treat, with worse clinical outcomes. Herein, we sought to develop a mouse model of GN-PJI to investigate the pathogenesis of these infections and identify potential therapeutic targets. An orthopedic-grade titanium implant was surgically placed in the femurs of mice, followed by infection of the knee joint with *Pseudomonas aeruginosa* or *Escherichia coli*. We found that in vitro biofilm-producing activity was associated with the development of an in vivo orthopedic implant infection characterized by bacterial infection of the bone/joint tissue, biofilm formation on the implants, reactive bone changes, and inflammatory immune cell infiltrates. In addition, a bispecific antibody targeting *P. aeruginosa* virulence factors (PcrV and Psl exopolysaccharide) reduced the bacterial burden in vivo. Taken together, our findings provide a preclinical model of GN-PJI and suggest the therapeutic potential of targeting biofilm-associated antigens.

Conflict of interest: LSM has received grant support from MedImmune for the work reported in this manuscript. LSM also has received grant support from Pfizer, Regeneron Pharmaceuticals, Moderna Therapeutics, and Boehringer Ingelheim; is on the scientific advisory board for Integrated Biotherapeutics; and is a shareholder of Noveome Biotherapeutics, and these associations are unrelated to the work reported in this manuscript. KPF is a paid employee of PerkinElmer, a company that provided bacterial strains (Xen14 and Xen41), from which the IVIS Lumina III imaging system was purchased. TSC, CT, LY, CKS, AD, and BRS are associated with MedImmune, a subsidiary of AstraZeneca, and may hold AstraZeneca stock.

Submitted: April 19, 2018
Accepted: July 26, 2018
Published: September 6, 2018

Reference information:
JCI Insight. 2018;3(17):e121737.
https://doi.org/10.1172/jci.insight.121737.

Introduction

Gram-negative (GN) prosthetic joint infections (PJI) represent an important and emerging clinical problem, but their pathogenesis is poorly understood. Historically, GN-PJI were considered a rare complication, accounting for 3%–6% of all PJI (1–3). However, during the past 15 years, reports from around the world have uncovered much higher rates of GN-PJI, ranging between 15 and 36 percent of all PJI (4–9). *Pseudomonas aeruginosa* and *Escherichia coli* were the most commonly reported infecting-organisms, and many cases were polymicrobial. As the number of primary and revision arthroplasties is projected to rise from the 1 million per year currently to nearly 4 million by 2030 in the US alone (10), clinicians will face an ever-growing burden of GN-PJI.

Despite this alarming increase in GN-PJI, little is known about the pathogenesis of these infections. This is disconcerting because GN-PJI caused by *P. aeruginosa* have a particularly high treatment failure rate and oftentimes require more surgeries and longer hospitalizations (11–14). To the best of our knowledge, preclinical animal models employed to investigate the pathogenesis of PJI have focused on Gram-positive (GP) bacteria, especially *Staphylococcus aureus* and *Staphylococcus epidermis* (15, 16). Therefore, there is a gap in knowledge and an unmet clinical need to elucidate the pathogenic mechanisms involved in GN-PJI, especially since GN bacteria differ from GP bacteria in many ways, including their mechanisms of virulence (17, 18), biofilm formation (19, 20), and host immune responses (21–23). Moreover, carbapenem-resistant and

extended-spectrum β-lactamase–producing (ESBL-producing) GN bacteria represent serious public health threats, as effective antibiotic options are becoming substantially more limited (24). In comparison, vancomycin and newer antibiotics (e.g., daptomycin and linezolid) have remained effective against antibiotic-susceptible and antibiotic-resistant GP bacteria, such as methicillin-resistant *S. aureus* (MRSA) (25). A greater understanding of the bacterial virulence mechanisms involved in GN-PJI is essential to guide the development of nonantibiotic alternatives to prevent and/or treat these difficult infections.

In the present study, we set out to develop a mouse model of GN-PJI to evaluate the pathogenesis of a more virulent infection caused by *P. aeruginosa*, which results in worse clinical outcomes, and a less virulent infection caused by *E. coli* (11–14). In addition, since GN-PJI caused by *P. aeruginosa* are especially problematic, this model was employed to assess the potential efficacy of a bispecific antibody targeting PcrV and Psl exopolysaccharide, key *P. aeruginosa* virulence factors thought to be involved in colonization and persistence involved in biofilm formation (26–29).

Results

Development of a mouse model of GN-PJI. To study the pathogenesis of a GN-PJI, we modified a previously described model of a GP-PJI (30–32). This was accomplished by surgically placing an orthopedic-grade titanium Kirschner-wire into the right femurs of C57BL/6 mice, with the end protruding into the knee joint, followed by bacterial inoculation before closure. We first performed experiments to determine the optimal inoculum for each bacterium by evaluating 3 different inocula (1×10^3, 1×10^4, and 1×10^5 CFU) of bioluminescent *P. aeruginosa* (Xen41) or *E. coli* (Xen14) strains that were pipetted into the exposed knee joints. The specific *P. aeruginosa* (Xen41) or *E. coli* (Xen14) strains used were previously reported to have biofilm-producing activity in vitro (33). To noninvasively monitor the in vivo bacterial burden, in vivo bioluminescence imaging (BLI) signals were measured on days 0, 1, 3, 7, 14, and 21 days, and ex vivo CFU were enumerated on bone/joint tissue and implants harvested on day 21, as previously described (31, 32). For *P. aeruginosa*, the 1×10^4 CFU inoculum was chosen for subsequent experiments because the in vivo BLI signals were present for the entire 21-day course of infection, and there was no mortality (Supplemental Figures 1 and 2; supplemental material available online with this article; https://doi.org/10.1172/jci.insight.121737DS1). In contrast, for *P. aeruginosa*, the 1×10^3 CFU inoculum resulted in in vivo BLI signals that decreased close to background levels before the end of the experiment on day 21, and the 1×10^5 CFU inoculum resulted in mortality in some of the mice. For *E. coli*, the 1×10^5 CFU inoculum was chosen to be used in subsequent experiments because the in vivo BLI signals were present for the entire 21-day course of infection, and there was no mortality observed. In contrast, the 1×10^3 or 1×10^4 CFU inocula for *E. coli* resulted in clearance of the infection by day 21 in all mice, as determined by in vivo BLI signals and ex vivo CFU counting.

In vivo and ex vivo bacterial burden in GN-PJI. For *P. aeruginosa*, the in vivo BLI signals of the 1×10^4 CFU inoculum peaked on day 3 ($9.5 \times 10^4 \pm 2.2 \times 10^4$ photons/s/cm^2/steradian) and decreased thereafter to a level that was statistically greater than the signals of uninfected control (sham surgery) mice and remained approximately a log above the background limit of detection (LOD) (Figure 1, A and B). For *E. coli*, the in vivo BLI signals of the 1×10^5 CFU inoculum peaked on day 1 ($9.5 \times 10^4 \pm 3.3 \times 10^4$ photons/s/cm^2/steradian, which was similar to the peak signal intensity observed with *P. aeruginosa*) and decreased to a level that was statistically greater than the signals of uninfected control mice, but they were only about a half-log above the LOD. Over the course of the experiment, the in vivo BLI signals of *P. aeruginosa* were statistically greater than the signals of *E. coli*. In vivo BLI signals of uninfected control mice remained below the LOD for the entire experiment. On day 21, mice were euthanized, and knee bone/joint tissues and implants were harvested to enumerate CFU from the tissue and sonicated implants. *P. aeruginosa*–infected mice had a mean of $3.3 \times 10^5 \pm 0.7 \times 10^5$ CFU from tissue samples (with all having at least 1.3×10^5 CFU) and a mean of $4.4 \times 10^2 \pm 1.6 \times 10^2$ CFU from the implants (Figure 1, C and D). In contrast, *E. coli*–infected mice had a mean of $3.1 \times 10^4 \pm 2.7 \times 10^4$ CFU from the tissue samples (with more than half of the mice having no detectable CFU) and no detectable CFU from the implants, both statistically lower than the tissue and implant CFU of *P. aeruginosa*–infected mice. Uninfected control mice had no detectable CFU from the tissue samples or implants.

To determine whether there were any remaining CFU, the tissue samples and implants were then cultured in shaking broth for an additional 48 hours followed by overnight culture on plates, and the presence or absence of bacterial growth was determined. For *P. aeruginosa*–infected mice, all 15 of 15 tissue samples and implants had bacterial growth. For *E. coli*–infected mice, 10 of 15 tissue samples (67%) and only 1 of 15 implants (7%) had bacterial growth; bacterial growth in both was significantly lower than the

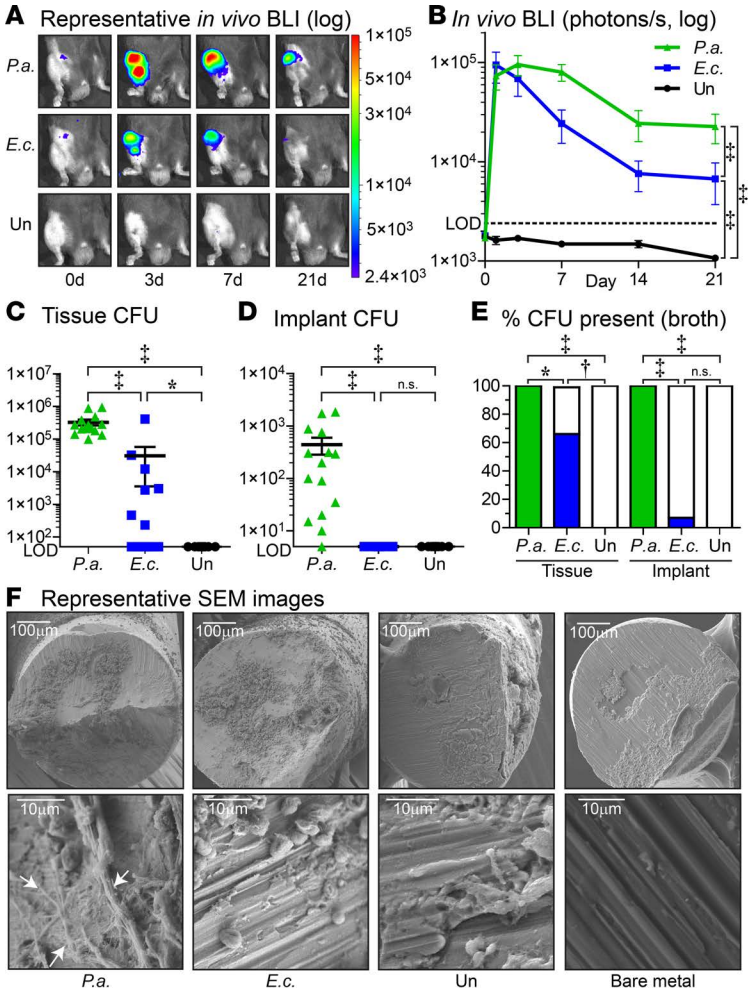

Figure 1. In vivo and ex vivo bacterial burden and biofilm formation in the Gram-negative prosthetic joint infection model. The in vivo mouse model of Gram-negative prosthetic joint infection (GN-PJI) was performed with bioluminescent strains of *P. aeruginosa* (*P.a.*) (n = 15), *E. coli* (*E.c.*) (n = 15), or no bacteria (Un, uninfected) (n = 20). (**A**) Representative in vivo BLI images. (**B**) Mean in vivo BLI signals quantified as maximum flux (photons/s/cm^2/steradian) ± SEM. (**C** and **D**) Mean CFU ± SEM recovered from tissue samples (**C**) and implants (**D**). (**E**) Percentage of tissue and implant samples with the presence of bacterial growth. (**F**) Representative low- (scale bars: 100 μm) and high-magnification (scale bars: 10 μm) scanning electron microscopy images of the intra-articular portion of the implant (n = 5/group), including bare metal image (implant surface prior to implantation). White arrows, characteristic viscous fibers seen in bacterial biofilms. LOD, limit of detection. $^*P < 0.05$, $^\dagger P < 0.01$, $^\ddagger P < 0.001$ between indicated groups, as calculated by using the AUC for each animal, with the AUC values then analyzed by a 1-way ANOVA model with heterogeneous within-group variance (**B**), nonparametric Kruskal-Wallis Dunn's test (**C** and **D**), or Fisher's exact test (**E**) (P values from multiple comparisons were adjusted by step-up Bonferroni method).

presence of bacterial growth from the respective tissue samples and implants from *P. aeruginosa*–infected mice (Figure 1E). Uninfected control mice had no bacterial growth from the tissue samples or implants.

Biofilm formation on implants in GN-PJI. To evaluate for biofilm formation on the implants, day 21 implants were harvested and fixed for scanning electron microscopy. On implants from *P. aeruginosa*–infected mice, substantial biofilm formation was visualized on the intra-articular end of the implant, with the characteristic viscous fibers covering the metal surface as well as adherent host immune cells (Figure 1F). In comparison, implants from *E. coli*–infected or uninfected mice demonstrated only adherent host immune cells with no discernible biofilm formation, similar to the bare metal surface of an implant prior to implantation.

Reactive bone changes and inflammation in GN-PJI. In our prior work using a mouse model of GP-PJI, progression of the infection over time resulted in expansion of the distal femur due to chronic reactive bone remodeling (32). To evaluate for similar expansion of the distal femur in response to a GN-PJI, anteroposterior X-rays of the distal femur were obtained on day 21, and distal femoral width and area were measured (Figure 2A). The distal femoral width of *P. aeruginosa*–infected mice had a mean of 3.8 ± 0.2 mm, which was significantly greater than the femoral width of *E. coli*–infected (mean 3.1 ± 0.1 mm) and uninfected mice (mean 3.0 ± 0.1 mm) (Figure 2B). The distal femoral areas of *P. aeruginosa*–infected mice had a mean value of 17.3 ± 0.7 mm^2, which was significantly greater than the femoral areas of *E. coli*–infected (mean 15.5 ± 0.4 mm^2) and uninfected mice (mean 14.1 ± 0.4 mm^2). The slightly increased femoral width but not the femoral area of *E. coli*–infected mice was statistically greater than uninfected mice.

To further measure the degree of inflammation at the site of the GN-PJI, [^{18}F]-fluoro-deoxy-glucose ([^{18}F]-FDG) PET imaging was employed. Although [^{18}F]-FDG is taken up by bacteria via glucose transporters (34), prior reports that compared sites of sterile inflammation with infection revealed very small differences, indicating that most of the [^{18}F]-FDG signals are from host inflammatory cells, such as neutrophils

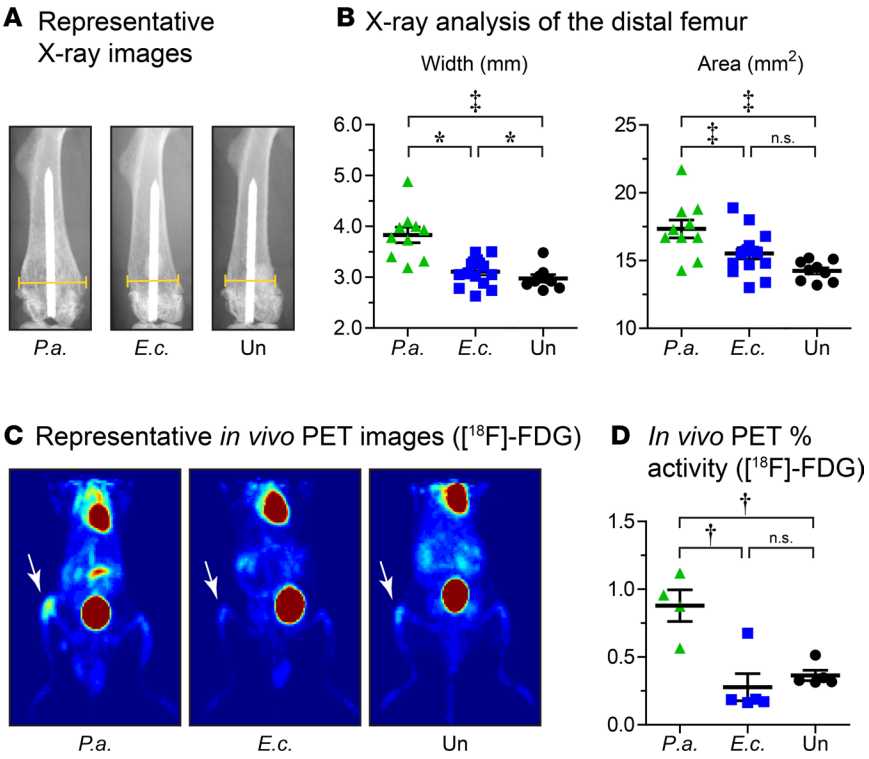

Figure 2. Reactive bone changes and inflammation in the Gram-negative prosthetic joint infection model. The in vivo mouse model of Gram-negative prosthetic joint infection (GN-PJI) was performed with *P. aeruginosa* (*P.a.*) (n = 10), *E. coli* (*E.c.*) (n = 15), or no bacteria (Un, uninfected) (n = 9), and on day 21, X-ray images and PET images were obtained. (**A**) Representative anteroposterior X-ray images: yellow bars indicate femoral width. (**B**) Mean femoral width (mm) ± SEM and mean femoral area (mm^2) ± SEM. (**C**) Representative [^{18}F]-fluoro-deoxy-glucose ([^{18}F]-FDG) maximum intensity projections of in vivo PET imaging (white arrows indicate surgical knee). High [^{18}F]-FDG emission in heart and bladder are expected. (**D**) Percentage injected activity per gram of [^{18}F]-FDG ± SEM at the surgical site with *P. aeruginosa* (n = 4), *E. coli* (n = 5), or no bacteria (n = 5). $^*P < 0.05$, $^\dagger P < 0.01$, $^\ddagger P < 0.001$ between indicated groups, as calculated by 1-way ANOVA model with heterogeneous within-group variance (P values from multiple comparisons were adjusted by step-up Bonferroni method) (**B** and **D**).

and monocytes, which are highly metabolically active and consume large quantities of glucose (35–37). On day 21, in *P. aeruginosa*–infected mice, the [^{18}F]-FDG percent activity per gram of tissue (0.88% ± 0.12%) was significantly and nearly 3-fold higher than that of *E. coli*–infected mice (0.28% ± 0.10%) and uninfected mice (0.36 ± 0.04%) (Figure 2, C and D). The [^{18}F]-FDG percent activity per gram of tissue for *E. coli*–infected mice was not significantly different from uninfected mice. Taken together, *P. aeruginosa* induced more substantial bone expansion and inflammation at the infection site than *E. coli*.

Similarly, day 21 histology of *P. aeruginosa*–infected mice revealed marked reactive bone changes within the cortical bone and physis and expansion of the cortical width at the distal end of the femurs adjacent to the site of biofilm formation on the implants (Figure 3, A–C). In addition, there were increased inflammatory immune infiltrates in the joint tissue (indicative of septic arthritis) and especially in the bone marrow cavity surrounding the implant site (indicative of osteomyelitis) (Figure 3D). In contrast, *E. coli*–infected mice had less expansion of the distal femurs, with more intact dense cortical bone and fewer reactive changes of the physis, along with fewer inflammatory cells in the bone marrow cavity, more closely resembling the histologic findings in uninfected control mice.

Inflammatory cell infiltrates in GN-PJI. To evaluate the specific composition of the immune cell infiltrates in the joint tissue, flow cytometry was performed on homogenized joint tissue specimens, as previously described in a model of GP-PJI (38). *P. aeruginosa*–infected mice, *E. coli*–infected mice, and uninfected mice all had neutrophil (Ly6G^{hi} Ly6C^{lo}) numbers and percentages that were not significantly different from each other (Figure 4). However, *P. aeruginosa*–infected mice had increased numbers and percentages of monocytes (Ly6G^{lo}Ly6C^{hi}) and macrophages (CD11b$^+$F4/80$^+$) compared with uninfected mice. In contrast, *E. coli*–infected mice had significantly increased numbers but not percentages of monocytes compared with uninfected mice. The numbers and percentages of macrophages in *E. coli*–infected mice were not statistically different from uninfected mice. These results suggest that by day 21 there was more of a chronic inflammatory response in the *P. aeruginosa*–infected mice, given that they had increased monocyte and macrophage infiltrates, while neutrophil infiltrates associated with acute infection and inflammation were similar among the groups. Overall, *E. coli* infection did not lead to a chronic inflammatory state. It should also be noted that, in this model of GN-PJI, we did not observe a population of Ly6G^{hi}Ly6C^{hi} myeloid-derived suppressor cells (Figure 4A), which have been previously reported to occur in GP-PJI mouse models with *S. aureus* (38).

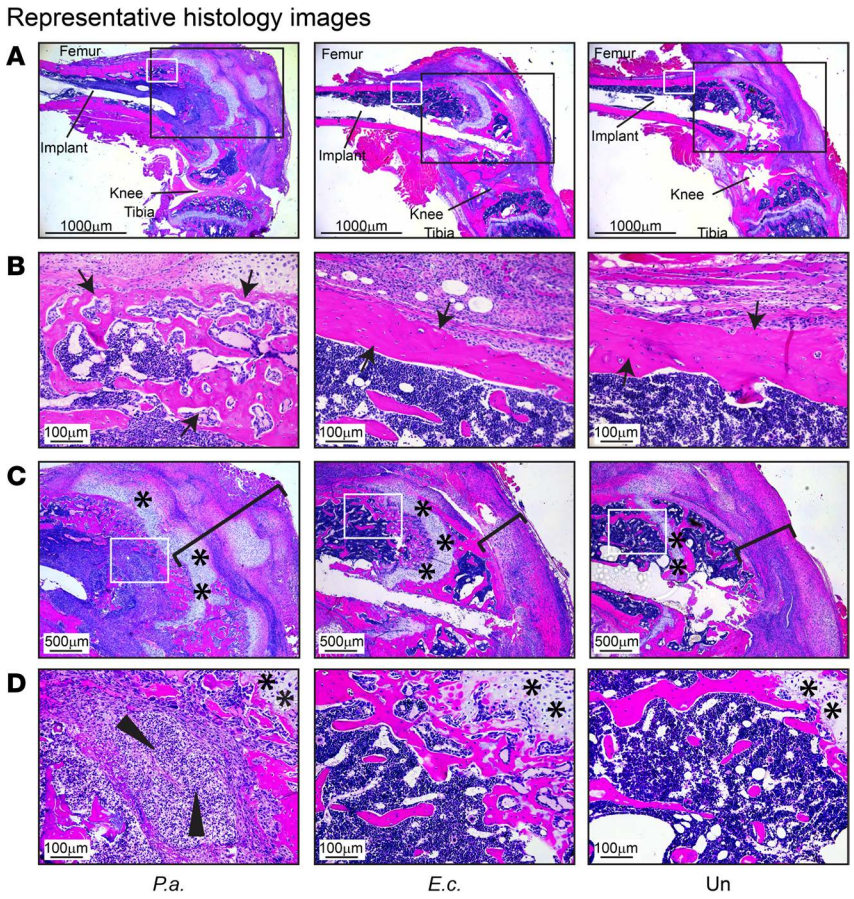

Figure 3. Histologic analysis in the Gram-negative prosthetic joint infection model. The in vivo mouse model of Gram-negative prosthetic joint infection (GN-PJI) was performed with *P. aeruginosa* (*P.a.*), *E. coli* (*E.c.*), or no bacteria (Un, uninfected) (n = 5/group). (**A**) Representative H&E-stained histologic sagittal sections in the plane of the maximum anteroposterior diameter of the location of the implant at day 21 after infection (scale bars: 1,000 μm). (**B**) Higher magnification of the white boxed area in **A**: black arrows indicate cortical bone surrounding the implant site (scale bars: 100 μm). (**C**) Higher magnification of the black boxed areas in **A**: asterisks indicate physis (growth plate) and brackets indicate bone width of the distal end of the femur (scale bars: 500 μm). (**D**) Higher magnification of the white boxed area in **C**: black arrowheads indicate inflammatory infiltrate in the bone (i.e., osteomyelitis) (scale bars: 100 μm).

In vitro biofilm-producing activity corresponds to the development of GN-PJI in vivo. The results in Figures 1–4 indicate that there was increased bacterial burden, biofilm formation, reactive bone changes, and inflammation in *P. aeruginosa*–infected mice compared with *E. coli*–infected mice, suggesting that *P. aeruginosa* was more virulent in this mouse model of GN-PJI. However, *E. coli* basically did not cause a productive infection in this GN-PJI. These results were somewhat unexpected because both *P. aeruginosa* and *E. coli* are the most common GN bacteria that cause PJI in humans (4–9). Although a prior report employed the same bioluminescent *P. aeruginosa* (Xen41) and *E. coli* (Xen14) strains used in this study in in vitro biofilm assays and indicated that both strains induced biofilms (33), we decided to directly quantify and compare the biofilm-producing activity of these strains as well as additional *E. coli* strains. An established in vitro biofilm assay was performed as previously described (39). The additional *E. coli* strains that we evaluated were the well-characterized reference strains 25922 and K12, as well as strain 836, a randomly chosen ESBL-producing strain from a patient with a urinary tract infection at the Johns Hopkins Hospital in 2013 (40). *P. aeruginosa* strain Xen41 had significantly increased in vitro biofilm formation compared with all of the *E. coli* strains (Figure 5A). However, among the *E. coli* strains, strain 25922 exhibited increased in vitro biofilm formation to nearly the same degree as *P. aeruginosa* and was significantly greater than *E. coli* strain Xen14. In contrast, *E. coli* strains K12 and 836 had less biofilm formation, similar to *E. coli* strain Xen14.

Based on these results, we reasoned that the relatively low in vitro biofilm-producing activity of Xen14 negatively affected the ability to induce the GN-PJI in vivo. We hypothesized that *E. coli* strains with increased in vitro biofilm formation would induce a more productive GN-PJI in vivo. To test this possibility, *E. coli* strain 25922 was used in the in vivo mouse model of GN-PJI at 1×10^5 CFU, the same inoculum used for *E. coli* strain Xen14. *E. coli* strain 25922–infected mice had markedly increased ex vivo CFU isolated from the tissue samples ($1.4 \times 10^6 \pm 0.5 \times 10^6$ CFU) and implants ($7.8 \times 10^2 \pm 3.0 \times 10^2$ CFU), with 100% of both tissue samples (15 of 15) and implants (10 of 10) having the presence of bacterial growth after broth culture (Figure 5, B–D). In addition, *E. coli* strain 25922–infected mice had mean values for femoral width (mean 4.0 ± 0.1 mm) and area (mean 18.0 ± 0.6 mm^2) by X-ray

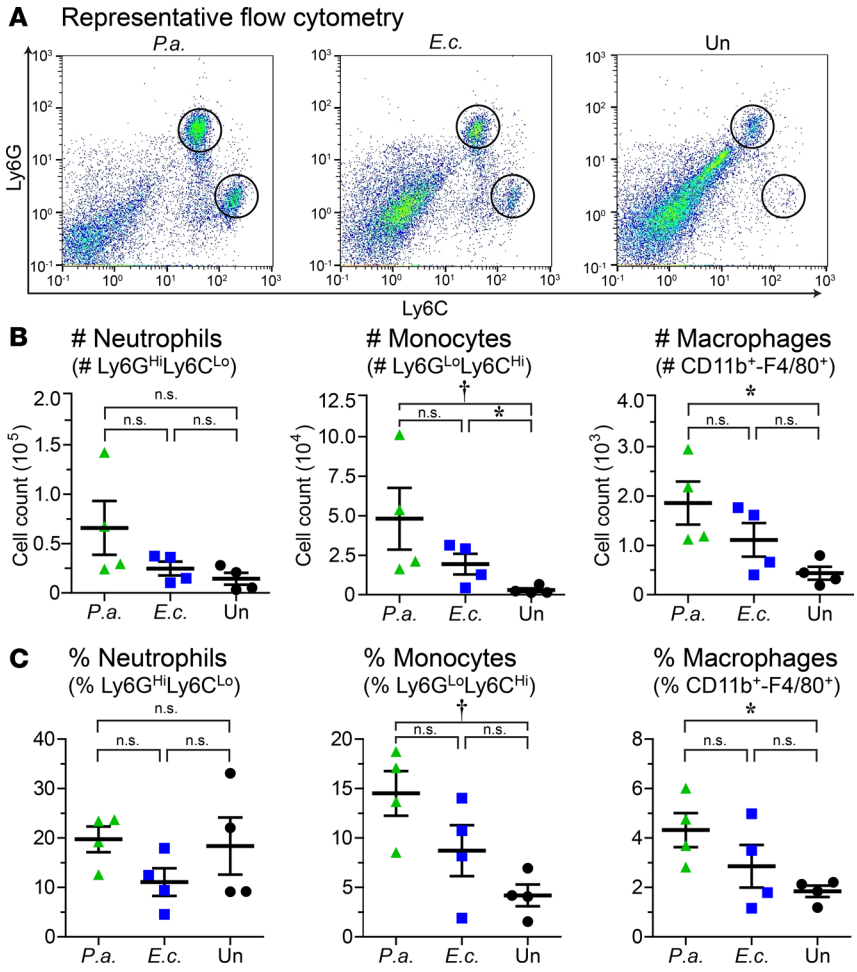

Figure 4. Flow cytometry for inflammatory cells in the Gram-negative prosthetic joint infection model. The in vivo mouse model of Gram-negative prosthetic joint infection (GN-PJI) was performed with *P. aeruginosa* (*P.a.*), *E. coli* (*E.c.*), or no bacteria (Un, uninfected) (n = 4/group). Representative flow plots (**A**), mean cell number ± SEM (**B**), and percentage of CD11b$^+$ cells ± SEM (**C**) in infected joint specimens obtained at day 21 after surgery. *$P < 0.05$, †$P < 0.01$ between indicated groups, as calculated by 1-way ANOVA model with heterogeneous within-group variance (P values from multiple comparisons were adjusted by step-up Bonferroni method).

analysis that were significantly greater compared with uninfected mice (Figure 5, E and F) as well as readily detectable biofilm formation on the implants (Figure 5G). Taken together, the enhanced in vitro biofilm-producing activity of *E. coli* strain 25922 led to a much more robust GN-PJI in vivo than *E. coli* strain Xen14. In addition, all of these results with *E. coli* strain 25922 closely resembled those observed in the *P. aeruginosa*–infected mice (Figures 1 and 2).

Bispecific antibody targeting PcrV and Psl reduces P. aeruginosa GN-PJI in vivo. Since increased in vitro biofilm forming activity was associated with more productive infections in the in vivo mouse model of GN-PJI for both *P. aeruginosa* and *E. coli*, we hypothesized that targeted inhibition of bacterial mechanisms involved in biofilm production would offer a therapeutic benefit. Therefore, we evaluated the potential prophylactic therapeutic effect of a bispecific antibody (MEDI3902) targeting two biofilm-associated virulence factors of *P. aeruginosa*: (a) PcrV, a protein produced by the type III secretion system of *P. aeruginosa* bacteria that is associated with bacterial aggregation that facilitates biofilm formation (29, 41), and (b) an exopolysaccharide involved in biofilm formation and maintenance (41, 42). Of note, MEDI3902 had previously been shown to be highly effective in promoting *P. aeruginosa* bacterial clearance in mouse models of lung infection, thermal injury, and bacteremia (26, 43, 44). Furthermore, incubation of established *P. aeruginosa* biofilms in vitro with a monoclonal antibody targeting Psl along with exogenous human neutrophils resulted in disruption and clearance of bacteria from *P. aeruginosa* biofilms (45). However, to the best of our knowledge, whether antibody-mediated targeting of PcrV and Psl results in a therapeutic benefit during an in vivo implant-related biofilm infection is unknown.

Mice were treated prophylactically via retro-orbital vein injection with MEDI3902 or an isotype control antibody (Control Ab) prior to performing the *P. aeruginosa* in vivo mouse PJI model. Compared with the Control Ab, MEDI3902 resulted in a diminished infection, as indicated by significantly decreased in vivo BLI signals (Figure 6A) and ex vivo CFU isolated from the tissue and implants (Figure 6, B and C). The Control Ab was

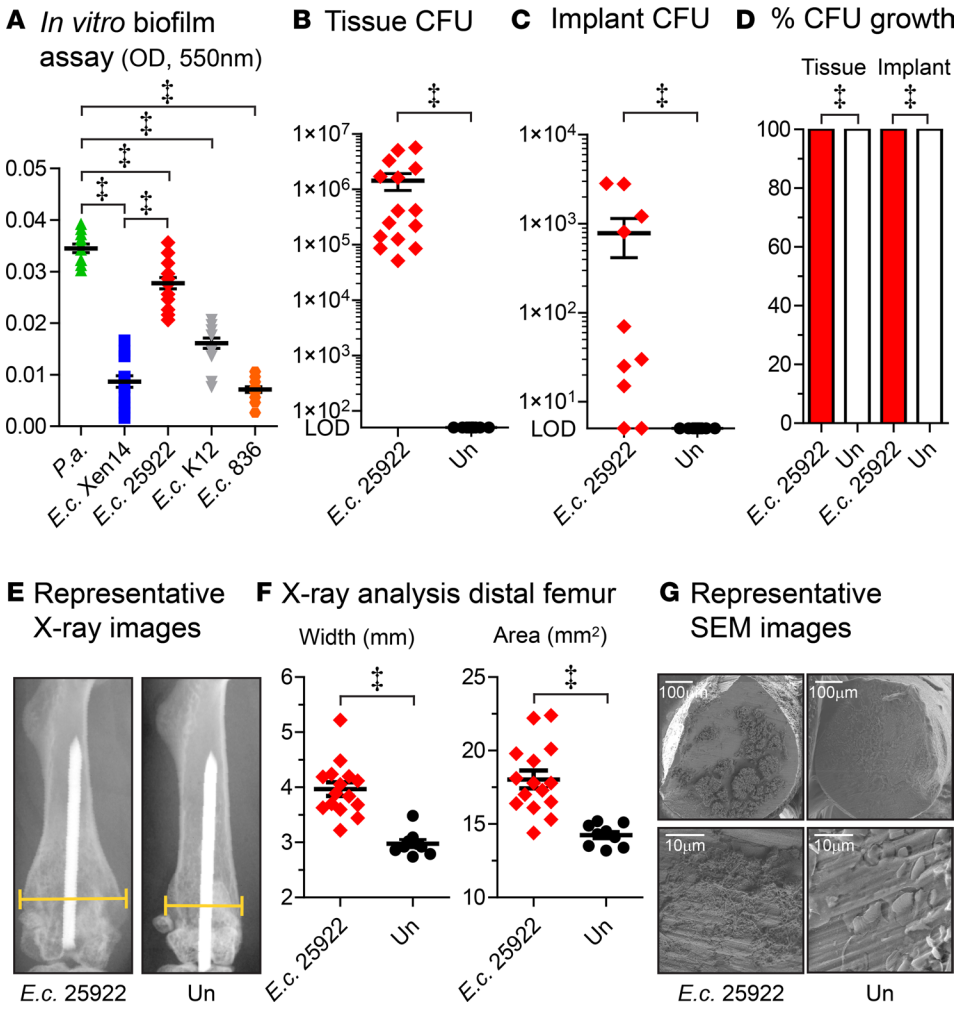

Figure 5. In vitro biofilm-producing activity and the development of an in vivo Gram-negative prosthetic joint infection. (**A**) In vitro biofilm formation of *P. aeruginosa* (*P.a.*) and *E. coli* (*E.c.*) strains in an in vitro microtiter biofilm assay, as measured by absorbance (550 nm) ± SEM (n = 15 replicate wells/strain). The in vivo mouse model of Gram-negative prosthetic joint infection (GN-PJI) was performed with a high in vitro biofilm-producing *E. coli* strain 25922 (*E.c.* 25922) or no bacteria (Un, uninfected). (**B** and **C**) Mean CFU ± SEM recovered from tissue samples for *E. coli* strain 25922 (*E.c.* 25922) (n = 15) vs. uninfected (n = 10) (**B**) and implants vs. uninfected (n = 10/group) (**C**). (**D**) Percentage of tissue and implant samples with the presence of bacterial growth using the groups from **B** and **C**. (**E**) Representative anteroposterior X-ray images: yellow bars indicate femoral width. (**F**) Mean femoral width (mm) ± SEM and mean femoral area (mm²) ± SEM (n = 10–15/group). (**G**) Representative low- (scale bars: 100 μm) and high-magnification (scale bars: 10 μm) scanning electron microscopy images of the intra-articular portion of the implant (n = 5/group). LOD, limit of detection. $^{\dagger}P < 0.01$, $^{\ddagger}P < 0.001$ between indicated groups, as calculated by 1-way ANOVA model with heterogeneous within-group variance (P values from multiple comparisons were adjusted by step-up Bonferroni method) (**A**), nonparametric exact Wilcoxon rank-sum test (**B** and **C**), Fisher's exact test (**D**), or two-sample t test (2 tailed) (**F**).

also compared with a sham injection of PBS (saline), and there were no significant differences in the in vivo BLI signals or ex vivo CFU from the tissue and implants (Supplemental Figure 3). Finally, to determine whether the antibodies accumulated at the site of infection, antibody levels of the MEDI3902 or the isotype Control Ab were measured in the bone/joint tissue homogenates at the end of the experiment on day 5. Both MEDI3902 and the isotype Control Ab accumulated at appreciable levels in the infected bone/joint tissue, which is consistent with the accumulation of antibodies at sites of inflammation and infection (46). However, there were lower levels of MEDI3902 than isotype Control Ab (Figure 6D), suggesting that MEDI3902 antibody bound to *P. aeruginosa* was cleared along with the bacteria in the treated mice.

Discussion

Increased understanding of the pathogenesis of GN-PJI to provide improved diagnostic and treatment options requires a reliable preclinical model. However, the only existing models in the literature to the best of our knowledge are those of GP-PJI (15, 16). Due to the many differences between virulence mechanisms and host-microbe interactions between GP and GN bacteria resulting in arguably fundamentally distinct types of infection (17–23), we sought to develop, characterize, and evaluate potential therapeutic targets in a preclinical mouse model of GN-PJI. We modified a previously described model of a GP-PJI (31, 32) in which an orthopedic-grade titanium Kirschner-wire was surgically placed in the femurs of mice followed by inoculation with *P. aeruginosa* or *E. coli* into the knee joint prior to closure. These GN bacteria were chosen since they represent more and less virulent causative pathogens, respectively, for GN-PJI in humans (4–9). In particular, we used the well-described bioluminescent *P. aeruginosa* Xen41 and *E. coli* Xen14 strains, as both had previously been reported to produce biofilms in vitro (33). Using this model, we uncovered several insights into the pathogenesis of GN-PJI.

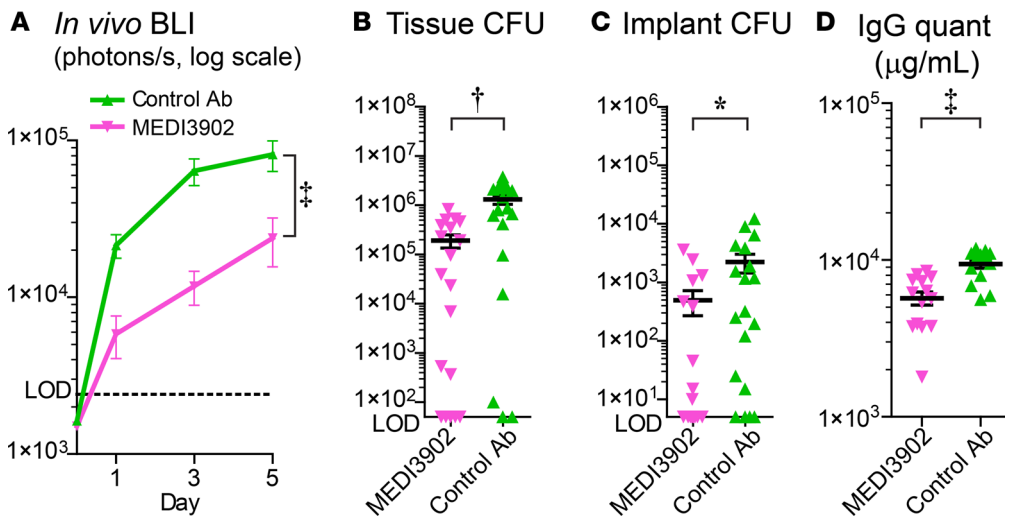

Figure 6. Targeting PcrV and Psl reduces *P. aeruginosa* Gram-negative prosthetic joint infection. A bispecific antibody targeting *P. aeruginosa* PcrV and Psl virulence factors associated with biofilm formation (MEDI3902) (n = 19) or an isotype control human IgG1 monoclonal antibody (Control Ab) (n = 19) was administered via the retro-orbital vein 1 day prior to performing the in vivo *P. aeruginosa*–PJI in vivo model. (**A**) Mean in vivo BLI signals quantified as maximum flux (photons/s/cm^2/steradian) ± SEM. (**B** and **C**) Mean CFU ± SEM recovered from tissue samples (**B**) and implants (**C**). (**D**) IgG quantification (μg/ml) of MEDI3902 (n = 14) and Control Ab (n = 14) levels in tissue homogenates obtained on day 5. LOD, limit of detection. $^*P < 0.05$, $^\dagger P < 0.01$, $^\ddagger P < 0.001$ between indicated groups, as calculated by using the AUC for each animal, with the AUC values then analyzed analyzed by a 1-way ANOVA model with heterogeneous within-group variance (**A**), nonparametric exact Wilcoxon rank-sum test (**B** and **C**) or 2-sample Student's t test (2 tailed) (**D**) (P values from multiple comparisons were adjusted by step-up Bonferroni method).

First, *P. aeruginosa* Xen41 was more virulent than *E. coli* Xen14 in the in vivo PJI model because *P. aeruginosa* (but not *E. coli*) resulted in mortality in a small fraction of the mice (Supplemental Figure 2). Therefore, the *P. aeruginosa* Xen41 strain was used at a log lower inoculum (1×10^4 CFU) than *E. coli* Xen14 (1×10^5 CFU). However, despite the lower inoculum, *P. aeruginosa* Xen41 resulted in greater bacterial burden in vivo and ex vivo, reactive bone changes, and inflammation at the site of infection than *E. coli* Xen14. Upon further study, *E. coli* strain Xen14 did not induce a productive biofilm infection in vivo, as there was no detectable ex vivo CFU isolated in half of the tissue samples, no bacterial growth from any of the cultured ex vivo implants, and no biofilm formation visualized on the implants. This result was somewhat surprising given the prevalence of *E. coli* as a pathogen for human GN-PJI (4–9). However, there might have been different biofilm-producing activity between *P. aeruginosa* Xen41 and *E. coli* Xen14 that could have affected the ability to produce the in vivo GN-PJI. Of note, *P. aeruginosa* Xen41 and *E. coli* Xen14 were both used in a single prior study to evaluate the efficacy of a salicylic acid–releasing catheter coating in inhibiting in vitro biofilms, but the relative biofilm-producing activities of Xen14 and Xen41 were not directly compared with each other (33).

Second, in directly evaluating the in vitro biofilm-forming activity of *P. aeruginosa* Xen41 and *E. coli* Xen14 as well as 3 other *E. coli* strains (25922 and K12 reference strains and the ESBL-producing strain 836, ref. 40) in an established in vitro microtiter biofilm assay (39), we found a broad range of biofilm-producing activity among the strains. *P. aeruginosa* and *E. coli* strain 25922 had the highest, whereas *E. coli* strains Xen14, K12, and 836 exhibited a substantially lower ability to form in vitro biofilms. These data provide a potential explanation for why *P. aeruginosa* Xen41 produced a more robust infection than *E. coli* strain Xen14 in our in vivo GN-PJI model.

Third, if biofilm-forming activity was a major factor for the development of a GN-PJI in vivo, we reasoned that *E. coli* strain 25922 would induce a more productive infection in this in vivo GN-PJI model. Indeed, *E. coli* strain 25922 resulted in increased ex vivo CFU from tissue samples and implants with marked reactive bone changes and readily visualized biofilm formation on the implants. These findings closely resembled the degree of infection in the in vivo GN-PJI infection with *P. aeruginosa* Xen41. Taken together, these data indicate that the in vitro biofilm-forming activity of *P. aeruginosa* and *E. coli* predicted virulence and disease severity in the in vivo GN-PJI model, which might also be a useful determinant to guide clinical treatment decisions. In addition, it is possible that the virulence of the pathogen also influenced local development and

systemic effects of the in vivo GN-PJI. For example, the high inoculum of *E. coli* strain 25922 (1×10^5 CFU) resulted in increased ex vivo CFU from the tissue samples ($1.4 \times 10^6 \pm 0.5 \times 10^6$ CFU), yet no mortality. In contrast, *P. aeruginosa* Xen41 at a lower inoculum (1×10^4 CFU) resulted in 5-fold fewer ex vivo CFU from the tissue samples ($3.3 \times 10^5 \pm 0.7 \times 10^5$ CFU).

Finally, to further evaluate the contribution of biofilm-forming activity to induce GN-PJI in vivo, we evaluated whether targeting bacterial factors involved in biofilm formation affected the infection. For these experiments, mice were prophylactically administered a bispecific antibody MEDI3902 against *P. aeruginosa* PcrV and Psl exopolysaccharide (26, 43, 44) prior to performing the in vivo *P. aeruginosa*–PJI model. MEDI3902 resulted in nearly a 10-fold decrease in the in vivo and ex vivo bacterial burden. These findings suggest that PcrV and Psl are important in the pathogenesis of implant-related biofilm infection in an in vivo setting and that they could represent therapeutic targets for PJI and other implant-related biofilm infections caused by *P. aeruginosa*. The specific targeting of PcrV is particularly relevant because the type III secretion system and production of PcrV might be important in the initial bacterial aggregation that facilitates biofilm formation (29, 41). In addition, the exopolysaccharide Psl is involved in the formation of *P. aeruginosa* biofilms in vitro (41), and a prior in vivo study found that a Psl deletion mutant *P. aeruginosa* strain resulted in less biofilm formation on a catheter infection model in vivo (42). Our findings are consistent with the previously reported biofilm-disrupting activity of an anti-Psl antibody in combination with neutrophils in vitro (45). Most importantly, MEDI3902 likely had therapeutic efficacy by targeting both PcrV and Psl in the in vivo GN-PJI model, which extends the previously reported activity of MEDI3902 against other in vivo models of *P. aeruginosa* infections in mice, including pneumonia, thermal injury, and bacteremia (26, 43, 44). Moreover, MEDI3902 had good tissue penetration in this GN-PJI model and, therefore, might be an attractive alternative against infections caused by antibiotic-resistant *P. aeruginosa* strains.

This study was limited in that a simplified implant was used rather than an actual prosthesis implanted in large animal or human PJI. However, this model was based on a previous model of GP-PJI that has been previously validated and is widely accepted in the literature (30–32, 38, 47–49). The original strain of low biofilm-producing *E. coli* (Xen14) was initially chosen for its purported biofilm-producing activity (33) and its bright in vivo BLI signals to noninvasively and longitudinally monitor the infectious course (50, 51). Comparison of in vivo BLI for the high biofilm-producing strain of *E. coli* (25922) with either *E. coli* Xen14 or *P. aeruginosa* Xen41 was not performed because the high biofilm-producing strain was not engineered to possess the bioluminescent *lux* construct. However, all other evaluated endpoints demonstrated that *P. aeruginosa* Xen41 and *E. coli* 25922 induced similar degrees of infection in the in vivo GN-PJI model, thus making such a comparison between the two strains feasible.

There are several future directions. We provided initial proof-of-concept efficacy data for targeted antibody therapy with MEDI3902 in this mouse model of *P. aeruginosa*–PJI. Additional work will involve evaluating more time points, changes in leukocyte cell infiltrates, and whether there is a therapeutic effect of administering MEDI3902 after the bacterial inoculation. In addition, previous work has shown that an anti-Psl antibody or MEDI3902 used adjunctively with standard of care antibiotics yields enhanced protective activity and bacterial clearance (26, 45). Therefore, we plan on evaluating the potential of MEDI3902 treatment with antibiotics in *P. aeruginosa*–PJI. Furthermore, given the variability in virulence among the *E. coli* strains, different strains of *P. aeruginosa* could also have varying degrees of virulence in this mouse model of GN-PJI. Therefore, we plan on comparing different *P. aeruginosa* clinical isolates and whether MEDI3902 has a similar therapeutic effect. However, it is expected that MEDI3902 will have broad efficacy against other *P. aeruginosa* strains, as we previously demonstrated in other in vivo mouse models of lung infection, thermal injury, and bacteremia (26, 43, 44).

In conclusion, a mouse model of GN-PJI established that *P. aeruginosa* and a high biofilm-producing *E. coli* strain induced a reliable implant-related biofilm infection in vivo, which allowed for insights into the pathogenesis of these infections. This model is unique compared with prior models of GP-PJI (15, 16) and is especially relevant, as GN bacteria are an important and increasingly common cause of PJI in humans (4–9). In addition, the efficacy of the bispecific antibody MEDI3902 in reducing the bacterial burden indicates that PcrV, Psl, or both are important factors in the pathogenesis of an implant-related biofilm infection in vivo and suggests MEDI3902 could be used as a nonantibiotic prophylactic and/or treatment approach. This is highly desirable because MEDI3902 would maintain activity against antibiotic-resistant *P. aeruginosa* strains without increasing the spread of antibiotic resistance or altering the composition of the beneficial microbiota (52). With the increasing incidence of GN-PJI, future studies are warranted to

further investigate GN-PJI in the mouse model presented herein and in other orthopedic implant infections involving larger animal models and humans.

Methods

P. aeruginosa and E. coli strains. Bacteria strains used include *P. aeruginosa* strain Xen41 (parent strain is the well-characterized PAO1 reference strain) and *E. coli* strain Xen14 (parent strain is WS2572, a well-characterized clinical isolate from the Weihenstephan Culture Collection, Munich Technical University) (PerkinElmer) (50), which both produce biofilms in vitro (33). Additional *E. coli* strains that were used include the reference strains 25922 (isolated from a patient in Seattle, Washington, USA, in 1946) (ATCC) and K12 (isolated from a patient stool sample in 1922) (ATCC) as well as 836, an ESBL-producing strain from a patient with a urinary tract infection at the Johns Hopkins Hospital in 2013 (40).

Bacterial preparation. *P. aeruginosa* and *E. coli* strains were streaked onto plates containing Luria-Bertani (LB) broth plus agar (1.5%) (Becton Dickinson). Colonies were grown overnight in LB broth at 37°C with shaking at 240 rpm, followed by 2.5-hour subcultures at 1:50 dilution to obtain midlogarithmic phase bacteria that were washed and reconstituted in sterile PBS. To determine the optimal inocula for *P. aeruginosa* Xen41 and *E. coli* Xen14 for the in vivo model of GN-PJI (see below), inocula of 1×10^3, 1×10^4, and 1×10^5 CFU were compared (Supplemental Figures 1 and 2); *P. aeruginosa* Xen41 at an inoculum of 1×10^4 CFU and *E. coli* Xen14 (and strain 25922) at an inoculum of 1×10^5 CFU were used in subsequent experiments.

Mice. Male C57BL/6 mice aged 6–8 weeks (Jackson Laboratories) were used in all experiments. All mice were bred and maintained under specific pathogen–free conditions at an animal facility accredited by the American Association for the Accreditation of Laboratory Animal Care at Johns Hopkins and housed according to procedures described in the *Guide for the Care and Use of Laboratory Animals* (National Academies Press, 2011).

In vivo model of GN-PJI. Mice underwent surgical implantation of a Kirschner-wire implant into the right knee joint as previously described (30–32). Briefly, mice were anesthetized with 2% isoflurane, and a medial parapatellar approach was used. The patella was dislocated laterally to gain access to the distal femur. The medullary canal was then reamed retrograde with a 25-gauge needle, and a 0.5 mm × 9 mm titanium Kirschner-wire (Modern Grinding) was inserted in a retrograde fashion into the distal femur. Approximately 0.5 mm was left protruding into the knee joint, onto which was directly pipetted 2 μl of the selected inocula of *P. aeruginosa* or *E. coli* bacteria or sterile PBS for uninfected control mice. The patella was carefully relocated, and the surgical incision was closed using two interrupted absorbable sutures.

In vivo BLI. In vivo BLI was performed using an IVIS Lumina III imaging system (PerkinElmer) as previously described (30–32). Imaging was performed immediately before (day 0) and then 1, 3, 7, 14, and 21 days after surgery. Mice were axially rotated within the chamber such that the right (surgical) leg was elevated 45 degrees from the horizontal. Bioluminescence was measured via maximum flux (photons/s/cm^2/steradian) obtained over a 5-minute period using large binning within a region of interest of 0.75 cm × 0.5 cm centered over the surgical leg. The LOD was 2.4×10^3 photons/s/cm^2/steradian.

Ex vivo bacterial quantification. On day 21, mice were euthanized and tissue samples from the proximal tibia through the midshaft of the femur were harvested and the implants were meticulously extracted as previously described (30–32). Bacterial CFU were isolated from the tissue samples by homogenizing (Pro200 Series homogenizer; Pro Scientific) in PBS on ice. Bacterial CFU were isolated from the implants by vortexing for 2 minutes before and after sonicating the implants in a 0.3% Tween solution (MilliporeSigma) for 10 minutes to dislodge any bacteria embedded within biofilm. Ex vivo CFU were enumerated using QuantityOne (Bio-Rad) after serially diluting the tissue homogenates or sonication solutions and overnight culture on LB plates. All individual colonies were assessed for BLI signals to exclude possible contaminants. To qualitatively determine the presence or absence of bacteria, the original tissue homogenates and sonicated solutions were incubated in LB broth for 48 hours at 37°C with shaking at 240 rpm. Bacterial growth was assessed by visual inspection of turbidity and then overnight culture on LB plates, which were also assessed for BLI signals to exclude possible contaminants.

Scanning electron microscopy. Implants were extracted on day 21 from crushed bone so as not to disturb the biofilm at the intra-articular end of the implant and were fixed in buffered 4% formaldehyde and 2.5% glutaraldehyde for 48 hours and rinsed with buffer 3 times (10 minutes each). Secondary fixation was performed for 1 hour in a PBS solution with 1% osmium tetraoxide. Dehydration using increasing levels of ethanol (30%, 50%, 67%, 80%, 90%, and 100% twice) was used for 15 minutes at each step. Implants were then transitioned through an increasing concentration of ethanol to hexamethyldisilazane (HMDS)

(ethanol/HMDS = 3:1, 1:1, 1:3) for 30 minutes each step, followed by pure HMDS for 15 minutes twice. Samples were air dried overnight to completely evaporate the HMDS. Implants were mounted on an aluminum block stub mounts and sputter-coated with gold-palladium. The entire intra-articular surface of the implant samples was imaged under a field emission scanning electron microscope (JSM-6700F FE-SEM; JEOL) at ×160 and ×1,000 magnification. Biofilm formation was deemed present upon visualization of characteristic viscous fibers.

X-ray imaging. On day 21, mice were euthanized and anteroposterior radiographs of the surgical knee were obtained using a Faxitron MX-20 (Faxitron Bioptics). Radiographs were then assessed using ImageJ (NIH). Maximum distal femoral width was determined by identifying the widest segment of bone perpendicular to the anatomical axis of the femur that was proximal to the fabella. Femoral length was measured via a line from the intercondylar notch to another line perpendicular to the anatomical axis of the femur that bisects the third trochanter. Distal femoral surface area was then calculated for the outer cortical area of the distal 50% of the femur; patella that were chronically dislocated on radiographs were not included in the overall outer cortical area.

Histological analysis. On day 21, mice were euthanized and implants were extracted from the midshaft of the femur so that minimal destruction of the distal aspect of the femur occurred. The knee bone/joint samples were fixed in 4% formalin overnight then decalcified and embedded within paraffin. The paraffin blocks were sectioned sagittally at 4-μm thickness, such that the microtome-cutting plane coincided with maximum anteroposterior diameter of the cylindrical implant. H&E-stained sections were evaluated by light microscopy, and photomicrographs were taken using a Leica DM4000 B LED light microscope mounted with a DFC495 camera (Leica Microsystems).

PET imaging. [^{18}F]-FDG PET imaging was performed as previously described (53). Briefly, clinical grade [^{18}F]-FDG was obtained from the Johns Hopkins PET Center Radiopharmacy, supplied by PETNET Solutions (Siemens Healthcare). Injectate was assayed using a sodium iodide CRC-15 dose calibrator and a calibration factor of 439 (Capintec). On day 21, mice were anesthetized with inhalation isoflurane (2%) and injected intravenously via the retro-orbital vein with 200 μCi average activity of tracer diluted to a final volume of 100 μl in isotonic saline. Following a 1-hour uptake period under continuous isoflurane anesthesia, mice were imaged using the MicroPET R4 system (Concorde Microsystems Inc.). Data sets were analyzed using ASIPro VM microPET analysis software (Siemens Preclinical Solutions). Volumes of interest (VOIs) were manually defined around the distal femur, and the percentage of activity per gram of tissue was calculated. In this study, we use the definition: percentage injected activity per gram = {[Activity in distal femur (μCi)/weight of VOI (gram)]/[injected activity (μCi)] × 100%}.

Flow cytometry. On day 21, mice were euthanized, and the surgical leg was harvested from the proximal tibia through the midshaft of the femur and the implant was carefully removed. Soft tissue around the distal femur and knee joint was passed through a 40-μm nylon cell strainer to create a single-cell suspension. Cells were pelleted at 376 *g* at 4°C for 8 minutes and then suspended and washed once in RPMI 1640 (Quality Biological Inc.) supplemented with 5% penicillin/streptomycin (Quality Biological) and 10% FBS (MilliporeSigma). Cells were resuspended in FACS buffer (Quality Biologicals) plus 1% BSA (MilliporeSigma) at 5×10^7 cells/ml. 100-μl aliquots were stained using anti-mouse antibodies against CD45-VioBlue (Miltenyi Biotec), Ly6G-PE (BD Biosciences), Ly6C-FITC (BD Biosciences), F4/80-PE-Cy7 (BD Biosciences), and CD11b-APC-Cy7 (BD Biosciences). Propidium iodide (Miltenyi Biotec) was added immediately before acquisition to exclude dead cells. Cells were acquired on a MACSQuant cytometer (Miltenyi Biotec) and analyzed using FlowJo software (Tree Star).

In vitro microtiter biofilm assay. The in vitro microtiter biofilm assay was performed according to previously described methods (39). Briefly, the bacterial strains were grown in tryptic soy broth (TSB) for 16 hours with shaking at 240 rpm. The overnight culture was diluted with 1% TSB supplemented with 0.2% glucose, and the bacterial concentration was adjusted to an optical density of 0.1 at 600 nm (OD600). 100 μl of each bacterial strain was added into each well of the round-bottom 96-well microtiter plates (Corning) and incubated at 37°C for 24 hours. Bacterial biofilm formation was measured after 3 washings with ddH_20, staining with crystal violet, 3 additional washings with ddH_20, destaining with acetic acid (30%), and finally reading the OD550. Identical results were obtained in this assay using LB broth.

In vivo administration of MEDI3902 or Control Abs. The bispecific antibody MEDI3902, which targets *P. aeruginosa* biofilm-related antigens PcrV and Psl, and a control anti-HIV IgG1 monoclonal antibody (R347) were obtained from MedImmune. MEDI3902 and the R347 Control Ab were diluted in sterile

PBS to a final concentration of 15 mg/kg and 11.7 mg/kg, respectively (calculated to have the same molecular weight as MEDI3902, which has a molecular weight of 200.3 kDa, whereas control IgG has a molecular weight of 150 kDa) and injected via the retro-orbital vein 1-day prior to performing the in vivo GN-PJI mouse model. For comparison, a sham injection of PBS (saline) was injected intravenously into mice as a no antibody control group.

Human antibody quantification from tissue homogenates. The concentration of MEDI3902 and Control Ab (R347) in tissue/bone homogenates was determined by ELISA. The procedure is a heterogeneous format in which wash steps follow after each incubation. All plates were washed 3 times with PBS supplemented with 0.1% Tween20. 96-well plates (NUNC MaxiSorp, ThermoFisher Scientific) were coated with 0.05 ml/well (0.5 mcg/ml) of sheep anti-human IgG (H+L) diluted in carbonate/bicarbonate buffer and incubated overnight at 4°C. Washed plates were blocked with assay buffer (PBS + 1% BSA) for 1 hour at room temperature. Antibodies prepared for the standard curve, quality controls, and samples were diluted appropriately in assay buffer, followed by addition of 0.05 ml to blocked plates. The plates were incubated at room temperature on a 96-well plate shaker at 350 rpm for 2 hours. After incubation, plates were washed followed by the addition of 0.05 ml goat anti-human IgG (H+L)-HRP (1:15,000) and incubated at room temperature with shaking for 30 minutes. Washed plates were developed with SureBlue Reserve (KPL SeraCare) (0.05 ml/well) for 5–15 minutes at room temperature followed by reaction termination with sulfuric acid (0.05 ml/well). Plates were read on a spectrophotometer at 450 nm, and data were analyzed with Soft Max Pro version 5.4 (Molecular Devices). The standard curve was established using a 4-parameter logistical curve fit model without weighting in SoftMax Pro (SMP) software. The nominal range of this assay was 1–1,000 ng/ml.

Statistics. Data for longitudinal comparisons were calculated by using the AUC for each animal, and then the AUC values were analyzed by a 1-way ANOVA model with heterogeneous within-group variance. Data for single time point comparisons across multiple groups (≥3 groups) were analyzed by nonparametric Kruskal-Wallis Dunn's test or a 1-way ANOVA model with heterogeneous within-group variance. For comparison between 2 groups, nonparametric exact Wilcoxon rank-sum test or 2-sample Student's *t* test (2 tailed) were performed. Fisher's exact test was applied for comparison between percentage values of cross tabulations. The specific tests performed are indicated in the figure legends. *P* values from multiple comparisons were adjusted by step-up Bonferroni method to control overall family-wise error rate. Statistical analysis were performed in SAS Studio 3.7 (SAS Institute Inc.), and figures were generated in Prism (GraphPad). Data are presented as mean ± SEM, and values of $P < 0.05$ were considered significant.

Study approval. All mice were bred and maintained under specific pathogen–free conditions at an animal facility accredited by the American Association for the Accreditation of Laboratory Animal Care at Johns Hopkins and housed according to procedures described in the *Guide for the Care and Use of Laboratory Animals* (National Academies Press, 2011). All animal studies were approved by the Johns Hopkins University Animal Care and Use Committee.

Author contributions

JMT, RJM, AGA, CAD, JEP, YW, RVO, LY, and AD performed experiments and analyzed data. JMT, RJM, RSS, KPF, NMB, TSC, CT, CKS, AD, BRS, DLJT, and LSM conceived the study, designed experiments, interpreted data, and wrote the manuscript.

Acknowledgments

This work was supported by grants T32AR07708 (to JMT and JEP) and R01AR073665 and R01AR069502 (to LSM) from the National Institute of Arthritis and Musculoskeletal and Skin Diseases from the US NIH and, in part, by a sponsored research agreement from MedImmune, through a Johns Hopkins-MedImmune Academic Industry Partnership. The content is solely the responsibility of the authors and does not necessarily represent the official views of the US NIH.

Address correspondence to: Lloyd S. Miller, Johns Hopkins Department of Dermatology, Cancer Research Building II, Suite 205, 1550 Orleans Street, Baltimore, Maryland 21231, USA. Phone: 410.955.8662; Email: lloydmiller@jhmi.edu.

1. Zimmerli W, Trampuz A, Ochsner PE. Prosthetic-joint infections. *N Engl J Med*. 2004;351(16):1645–1654.
2. Moran E, Masters S, Berendt AR, McLardy-Smith P, Byren I, Atkins BL. Guiding empirical antibiotic therapy in orthopaedics: The microbiology of prosthetic joint infection managed by debridement, irrigation and prosthesis retention. *J Infect*. 2007;55(1):1–7.
3. Del Pozo JL, Patel R. Clinical practice. Infection associated with prosthetic joints. *N Engl J Med*. 2009;361(8):787–794.
4. Benito N, et al. Etiology of surgical site infections after primary total joint arthroplasties. *J Orthop Res*. 2014;32(5):633–637.
5. Benito N, et al. Time trends in the aetiology of prosthetic joint infections: a multicentre cohort study. *Clin Microbiol Infect*. 2016;22(8):732.e1–732.e8.
6. Hsieh PH, Lee MS, Hsu KY, Chang YH, Shih HN, Ueng SW. Gram-negative prosthetic joint infections: risk factors and outcome of treatment. *Clin Infect Dis*. 2009;49(7):1036–1043.
7. Jamei O, et al. Which orthopaedic patients are infected with Gram-negative non-fermenting rods? *J Bone Jt Infect*. 2017;2(2):73–76.
8. Li GQ, Guo FF, Ou Y, Dong GW, Zhou W. Epidemiology and outcomes of surgical site infections following orthopedic surgery. *Am J Infect Control*. 2013;41(12):1268–1271.
9. Peel TN, Cheng AC, Buising KL, Choong PF. Microbiological aetiology, epidemiology, and clinical profile of prosthetic joint infections: are current antibiotic prophylaxis guidelines effective? *Antimicrob Agents Chemother*. 2012;56(5):2386–2391.
10. Kurtz S, Ong K, Lau E, Mowat F, Halpern M. Projections of primary and revision hip and knee arthroplasty in the United States from 2005 to 2030. *J Bone Joint Surg Am*. 2007;89(4):780–785.
11. Cunningham DJ, Kavolus JJ, Bolognesi MP, Wellman SS, Seyler TM. Specific infectious organisms associated with poor outcomes in treatment for hip periprosthetic infection. *J Arthroplasty*. 2017;32(6):1984–1990.e5.
12. Rodríguez-Pardo D, et al. Gram-negative prosthetic joint infection: outcome of a debridement, antibiotics and implant retention approach. A large multicentre study. *Clin Microbiol Infect*. 2014;20(11):O911–O919.
13. Shah NB, et al. Pseudomonas prosthetic joint infections: A Review of 102 Episodes. *J Bone Jt Infect*. 2016;1:25–30.
14. Zmistowski B, Fedorka CJ, Sheehan E, Deirmengian G, Austin MS, Parvizi J. Prosthetic joint infection caused by gram-negative organisms. *J Arthroplasty*. 2011;26(6 Suppl):104–108.
15. Carli AV, et al. Quantification of peri-implant bacterial load and in vivo biofilm formation in an innovative, clinically representative mouse model of periprosthetic joint infection. *J Bone Joint Surg Am*. 2017;99(6):e25.
16. Lovati AB, Bottagisio M, de Vecchi E, Gallazzi E, Drago L. Animal models of implant-related low-grade infections. A twenty-year review. *Adv Exp Med Biol*. 2017;971:29–50.
17. Cohen J. Mechanisms of tissue injury in sepsis: contrasts between gram positive and gram negative infection. *J Chemother*. 2001;13 Spec No 1(1):153–158.
18. Ramachandran G. Gram-positive and gram-negative bacterial toxins in sepsis: a brief review. *Virulence*. 2014;5(1):213–218.
19. López D, Vlamakis H, Kolter R. Biofilms. *Cold Spring Harb Perspect Biol*. 2010;2(7):a000398.
20. O'Toole G, Kaplan HB, Kolter R. Biofilm formation as microbial development. *Annu Rev Microbiol*. 2000;54:49–79.
21. Abe R, et al. Gram-negative bacteremia induces greater magnitude of inflammatory response than Gram-positive bacteremia. *Crit Care*. 2010;14(2):R27.
22. Skovbjerg S, et al. Gram-positive and gram-negative bacteria induce different patterns of cytokine production in human mononuclear cells irrespective of taxonomic relatedness. *J Interferon Cytokine Res*. 2010;30(1):23–32.
23. Takeuchi O, et al. Differential roles of TLR2 and TLR4 in recognition of gram-negative and gram-positive bacterial cell wall components. *Immunity*. 1999;11(4):443–451.
24. Doi Y, et al. Gram-negative bacterial infections: research priorities, accomplishments, and future directions of the Antibacterial Resistance Leadership Group. *Clin Infect Dis*. 2017;64(suppl_1):S30–S35.
25. Osmon DR, et al. Diagnosis and management of prosthetic joint infection: clinical practice guidelines by the Infectious Diseases Society of America. *Clin Infect Dis*. 2013;56(1):e1–e25.
26. DiGiandomenico A, et al. A multifunctional bispecific antibody protects against Pseudomonas aeruginosa. *Sci Transl Med*. 2014;6(262):262ra155.
27. Mikkelsen H, Sivaneson M, Filloux A. Key two-component regulatory systems that control biofilm formation in Pseudomonas aeruginosa. *Environ Microbiol*. 2011;13(7):1666–1681.
28. Patel A, et al. An engineered bispecific DNA-encoded IgG antibody protects against Pseudomonas aeruginosa in a pneumonia challenge model. *Nat Commun*. 2017;8(1):637.
29. Tran CS, et al. The Pseudomonas aeruginosa type III translocon is required for biofilm formation at the epithelial barrier. *PLoS Pathog*. 2014;10(11):e1004479.
30. Niska JA, Shahbazian JH, Ramos RI, Francis KP, Bernthal NM, Miller LS. Vancomycin-rifampin combination therapy has enhanced efficacy against an experimental Staphylococcus aureus prosthetic joint infection. *Antimicrob Agents Chemother*. 2013;57(10):5080–5086.
31. Pribaz JR, et al. Mouse model of chronic post-arthroplasty infection: noninvasive in vivo bioluminescence imaging to monitor bacterial burden for long-term study. *J Orthop Res*. 2012;30(3):335–340.
32. Thompson JM, et al. Oral-only linezolid-rifampin is highly effective compared with other antibiotics for periprosthetic joint infection: study of a mouse model. *J Bone Joint Surg Am*. 2017;99(8):656–665.
33. Nowatzki PJ, et al. Salicylic acid-releasing polyurethane acrylate polymers as anti-biofilm urological catheter coatings. *Acta Biomater*. 2012;8(5):1869–1880.
34. Heuker M, et al. In vitro imaging of bacteria using 18F-fluorodeoxyglucose micro positron emission tomography. *Sci Rep*. 2017;7(1):4973.
35. Ertay T, Sencan Eren M, Karaman M, Oktay G, Durak H. 18F-FDG-PET/CT in Initiation and Progression of Inflammation and Infection. *Mol Imaging Radionucl Ther*. 2017;26(2):47–52.
36. Sugawara Y, Gutowski TD, Fisher SJ, Brown RS, Wahl RL. Uptake of positron emission tomography tracers in experimental bacterial infections: a comparative biodistribution study of radiolabeled FDG, thymidine, L-methionine, 67Ga-citrate, and 125I-HSA. *Eur J Nucl Med*. 1999;26(4):333–341.
37. Yamada S, Kubota K, Kubota R, Ido T, Tamahashi N. High accumulation of fluorine-18-fluorodeoxyglucose in turpentine-induced

inflammatory tissue. *J Nucl Med*. 1995;36(7):1301–1306.
38. Heim CE, et al. Myeloid-derived suppressor cells contribute to Staphylococcus aureus orthopedic biofilm infection. *J Immunol*. 2014;192(8):3778–3792.
39. O'Toole GA. Microtiter dish biofilm formation assay. *J Vis Exp*. 2011;47(47):e2437.
40. Weinstein EA, et al. Imaging Enterobacteriaceae infection in vivo with 18F-fluorodeoxysorbitol positron emission tomography. *Sci Transl Med*. 2014;6(259):259ra146.
41. Mikkelsen H, Bond NJ, Skindersoe ME, Givskov M, Lilley KS, Welch M. Biofilms and type III secretion are not mutually exclusive in Pseudomonas aeruginosa. *Microbiology (Reading, Engl)*. 2009;155(Pt 3):687–698.
42. Cole SJ, Records AR, Orr MW, Linden SB, Lee VT. Catheter-associated urinary tract infection by Pseudomonas aeruginosa is mediated by exopolysaccharide-independent biofilms. *Infect Immun*. 2014;82(5):2048–2058.
43. Le HN, et al. MEDI3902 correlates of protection against severe Pseudomonas aeruginosa pneumonia in a rabbit acute pneumonia model. *Antimicrob Agents Chemother*. 2018;62(5):e02565–17.
44. Thanabalasuriar A, et al. Bispecific antibody targets multiple Pseudomonas aeruginosa evasion mechanisms in the lung vasculature. *J Clin Invest*. 2017;127(6):2249–2261.
45. Ray VA, et al. Anti-Psl targeting of Pseudomonas aeruginosa biofilms for neutrophil-mediated disruption. *Sci Rep*. 2017;7(1):16065.
46. Romero Pastrana F, et al. Noninvasive optical and nuclear imaging of Staphylococcus-specific infection with a human monoclonal antibody-based probe. *Virulence*. 2018;9(1):262–272.
47. Hegde V, et al. Single-dose, preoperative vitamin-d supplementation decreases infection in a mouse model of periprosthetic joint infection. *J Bone Joint Surg Am*. 2017;99(20):1737–1744.
48. Stavrakis AI, et al. In vivo efficacy of a "smart" antimicrobial implant coating. *J Bone Joint Surg Am*. 2016;98(14):1183–1189.
49. Wang Y, et al. Mouse model of hematogenous implant-related Staphylococcus aureus biofilm infection reveals therapeutic targets. *Proc Natl Acad Sci USA*. 2017;114(26):E5094–E5102.
50. Rocchetta HL, et al. Validation of a noninvasive, real-time imaging technology using bioluminescent Escherichia coli in the neutropenic mouse thigh model of infection. *Antimicrob Agents Chemother*. 2001;45(1):129–137.
51. Sharma PK, et al. Spatiotemporal progression of localized bacterial peritonitis before and after open abdomen lavage monitored by in vivo bioluminescent imaging. *Surgery*. 2010;147(1):89–97.
52. Goff DA, et al. A global call from five countries to collaborate in antibiotic stewardship: united we succeed, divided we might fail. *Lancet Infect Dis*. 2017;17(2):e56–e63.
53. Zoch ML, Abou DS, Clemens TL, Thorek DL, Riddle RC. In vivo radiometric analysis of glucose uptake and distribution in mouse bone. *Bone Res*. 2016;4:16004.